Statistical Analysis of Sodium Doppler Wind–Temperature Lidar Measurements of Vertical Heat Flux

LIGUO SU

Geophysical Institute, and Department of Electrical and Computer Engineering, University of Alaska Fairbanks, Fairbanks, Alaska

RICHARD L. COLLINS

Geophysical Institute, and Atmospheric Sciences Program, University of Alaska Fairbanks, Fairbanks, Alaska

DAVID A. KRUEGER AND CHIAO-YAO SHE

Department of Physics, Colorado State University, Fort Collins, Colorado

(Manuscript received 13 September 2006, in final form 12 April 2007)

ABSTRACT

A statistical study is presented of the errors in sodium Doppler lidar measurements of wind and temperature in the mesosphere that arise from the statistics of the photon-counting process that is inherent in the technique. The authors use data from the Colorado State University (CSU) sodium Doppler wind-temperature lidar, acquired at a midlatitude site, to define the statistics of the lidar measurements in different seasons under both daytime and nighttime conditions. The CSU lidar measurements are scaled, based on a 35-cm-diameter receiver telescope, to the use of large-aperture telescopes (i.e., 1-, 1.8-, and 3.5-m diameters). The expected biases in vertical heat flux measurements at a resolution of 480 m and 150 s are determined and compared to Gardner and Yang's reported geophysical values of 2.3 K m s^{-1}. A cross-correlation coefficient of 2%–7% between the lidar wind and temperature estimates is found. It is also found that the biases vary from -4×10^{-3} K m s^{-1} for wintertime measurements at night with a 3.5-m telescope to -61 K m s^{-1} for summertime measurements at midday with a 1-m telescope. During winter, at night, the three telescope systems yield biases in their heat flux measurements that are less than 10% of the reported value of the heat flux; and during summer, at night, the 1.8- and 3.5-m systems yield biases in their heat flux measurements that are less than 10% of the geophysical value. While during winter at midday the 3.5-m system yields biases in their heat flux measurements that are less than 10% of the geophysical value, during summer at midday all of the systems yield flux biases that are greater than the geophysical value of the heat flux. The results are discussed in terms of current lidar measurements and proposed measurements at high-latitude sites.

1. Introduction

Investigation of the mesosphere has been prompted by the fact that the region is maintained far from radiative equilibrium by dynamic and chemical heating effects (Andrews et al. 1987). Inertial gravity (or buoyancy) waves, with periods from several minutes to several hours and vertical wavelengths on order of kilometers, have been recognized as a major contribution to the general circulation of the middle atmosphere since the 1970s (Houghton 1978). These waves are primarily generated in the troposphere and propagate upward in the atmosphere. As they propagate through the middle atmosphere, gravity waves interact with other waves, tides, and mean winds. In these interactions, the gravity waves loose their energy and contribute to both the general circulation and the turbulent mixing and diffusion of constituents. Efforts to quantify the forcing of the circulation by gravity waves have generally employed the following three approaches: direct observations of the small-scale motions associated with these waves, atmospheric model studies that employ parameterizations of the wave forcing and are constrained by observations, and balance studies where the forcing that cannot be explained in terms of large-scale plan-

Corresponding author address: Richard L. Collins, Geophysical Institute, University of Alaska Fairbanks, 903 Koyukuk Drive, Fairbanks, AK 99775-7320.
E-mail: rlc@gi.alaska.edu

DOI: 10.1175/2007JTECHA915.1

etary waves is attributed to gravity waves [see discussion in recent collections of papers in the monographs edited by Johnson and Killeen (1995) and Siskind et al. (2000), and the review article by Fritts and Alexander (2003)].

The small-scale wave perturbations [i.e., three wind components (zonal, u'; meridional, v'; and vertical, w'), temperature (T'), and/or density (ρ')] typically represent relative perturbations of a couple of percent. Accurate measurement of these quantities has driven the development of lidar, radar, and airglow instruments that are capable of high-precision and high-resolution measurements of wind, temperature, and constituent concentrations. The accurate determination of the associated wave-generated momentum and heat fluxes (i.e., $\overline{u'w'}$, $\overline{v'w'}$, $\overline{w'T'}$), and the resultant forcing of the mean flow due to the vertical gradients in these fluxes, places even greater demands on the accuracy and precision of the measurements. Measurements of the momentum flux have attracted the most attention because the formulation of the gravity wave forcing arises in the momentum equations of the general circulation, and radar systems capable of measuring winds have been operated since the 1980s (Vincent and Reid 1983; Wang and Fritts 1990). However, determination of the fluxes is complicated by the large natural variability in the atmosphere (Kudeki and Franke 1998; Gardner and Yang 1998, hereafter GY98). Furthermore, Thorsen et al. (2000) studied the use of single instruments that make multiple line-of-sight velocity measurements to determine the momentum flux (i.e., $\overline{u'w'}$, $\overline{v'w'}$). Thorsen et al. found that the viewing geometry can bias the momentum flux estimate and should be carefully chosen based on the geophysical variability in the horizontal and vertical winds.

In principle, the measurement of heat fluxes does not suffer from these problems of measurement geometry, because a single-beam zenith-pointing lidar system is capable of common-volume temperature and vertical wind measurements along a single line of sight. The average heat flux associated with nonbreaking gravity waves that propagate freely, conserve their energy, and grow with altitude is identically zero. The net heat flux associated with breaking gravity waves can be viewed as having the following two components: heat flux associated with the turbulence generated by the waves, and wave flux convergence associated with breaking waves that no longer grow freely with altitude. The flux associated with breaking gravity waves is expected to be negative, and these wave motions are expected to cool the mesosphere while the turbulence that is generated results in heating (Schoeberl et al. 1983). Studies have shown that the cooling by the wave heat flux divergence is greater than the heating by the turbulence (Huang and Smith 1991; Becker 2004). Walterscheid (1981) has shown that wave breaking resulting from the Doppler shifting of waves by tides also yields a negative vertical heat flux. In comparison, aircraft measurements of eddy heat fluxes in the boundary layer, associated with atmospheric turbulence, show mostly small positive and negative values that average to near zero, with occasional positive spikes associated with convective plumes (Stull 1988).

Recently, several researchers have reported sodium Doppler wind–temperature lidar observations with large-aperture (>3 m) telescopes that have yielded high-resolution (2.5 min, 480 m) vertical wind and temperature measurements and estimates of the heat flux in the mesopause region (~80–100 km). GY98 reported a vertical heat flux associated with dissipating gravity waves of -2.29 ± 0.4 K m s^{-1} from 65 h of measurements employing the large-aperture telescope (3.5 m) at the Starfire Optical Range (SOR) in New Mexico (35°N, 107°W). Gardner et al. (2002) have subsequently reported a vertical heat flux associated with dissipating gravity waves of -1.55 ± 0.2 K m s^{-1} from over 200 h of measurements at SOR. Liu and Gardner (2005) reported a vertical heat flux associated with dissipating gravity waves of -1.40 ± 0.5 K m s^{-1} from over 100 h of measurements employing the large-aperture telescope (3.7 m) at the Advanced Electro-Optic System (AEOS) in Haleakala, Hawaii (21°N, 156°W). The value of these heat fluxes measured at SOR and AEOS correspond to wave-induced cooling rates of -30 to -50 K day^{-1}. GY98 presented an extensive analysis of the errors and uncertainties in the flux measurements, but did not consider the cross correlation between the errors, and concluded that the biases in the measured heat flux were of 8×10^{-5} K m s^{-1}. Given the extensive presentation, analysis, and discussion of the experimental technique by GY98, we compare the results of this study with the SOR measurements of GY98.

In this study we extend the analysis of GY98 to consider how the biases in the heat flux measurements vary with telescope aperture, geographic location, and season. The statistical quality of the lidar measurement improves with an increase in signal. The power–aperture product, effective backscatter cross section of the sodium atoms, and sodium concentration all combine to determine the magnitude of the lidar signal and the sensitivity and accuracy of the lidar system (see review by Chu and Papen 2005) The sodium concentration (and thus the amplitude of the lidar signal) varies with season, with a winter maximum and summer minimum and a more extreme variation at the poles than the equator (e.g., Gardner et al. 1988; Plane 1991;

Gardner et al. 2005). We use measurements from the Colorado State University (CSU) sodium Doppler wind–temperature lidar at Fort Collins, Colorado (41°N, 105°W; Arnold and She 2003) to prescribe the sodium concentrations and system performance under day- and nighttime conditions in both summer- and wintertime. We conduct a forward random variable analysis from the photon count signals as well as a Monte Carlo simulation to determine the expected biases in the flux measurements. We use these simulations to determine the range of geophysical conditions and telescope apertures that can be used to make reliable vertical heat flux measurements.

2. The sodium Doppler wind–temperature lidar measurement technique

a. Laser spectroscopy of sodium

Sodium resonance wind–temperature lidar systems use the sodium D_2 fluorescence from the mesospheric sodium layer to measure wind and temperature profiles in the mesopause region (~80–100 km). The width of the sodium spectrum varies with temperature and the relative position of the spectrum shifts with wind. The wind and temperature can be determined from the relative strength of the laser echo at different frequencies. The first measurements of temperature were reported in the late 1970s (Gibson et al. 1979), with subsequent measurements reported in the mid-1980s (Fricke and von Zahn 1985). Both of these early systems employed pulsed-dye lasers with tunable Fabry–Perot interferometers to transmit tunable narrowband laser light. Modern wind–temperature systems were developed using Doppler-free spectroscopy and pulsed-dye lasers seeded with continuous-wave ring-dye lasers in the 1990s (She et al. 1990; Bills et al. 1991; She and Yu 1995).

Several researchers have presented detailed reviews of the spectroscopy of sodium in the mesosphere (Fricke and von Zahn 1985; Bills et al. 1991; She et al. 1992; She and Yu 1995; Chu and Papen 2005). Some studies have modeled the sodium spectrum using the doublet fine structure (e.g., Bills et al. 1991), while others have used the complete hyperfine structure (e.g., Fricke and von Zahn 1985). We note that the doublet approximation for the sodium spectral shape yields differences of less than 0.5% in the estimated scattering cross sections. In this study we follow the approach of both She and Yu (1995) and Chu and Papen (2005), where we model the Doppler-broadened sodium line as the superposition of six hyperfine lines. We adopt the values for the spectroscopic parameters presented in Table 5.1 of Chu and Papen.

b. Lidar measurement of temperature and wind

For a lidar system employing a photon-counting detection system, we can express the expected total photon count $N_{\mathrm{TOT}}(z)$ from the altitude range $(z - \Delta z/2, z + \Delta z/2)$ in a time interval Δt as the sum of three terms,

$$N_{\mathrm{TOT}}(z) = N_S(z) + N_B + N_D, \tag{1}$$

where $N_S(z)$ represents the signal detected from the scatterers at altitude z, N_B represents the signal due to background skylight conditions, and N_D represents the signal due to detector noise. We can express these terms as

$$N_S(z) = \eta\tau_L\tau_R\left(\frac{E_L R_L \Delta t}{h\upsilon_L}\right)[\sigma_{\mathrm{eff}}(\upsilon_L, T, V)\rho(z)\Delta z] \times \left(\frac{A_R}{4\pi z^2}\right), \tag{2}$$

$$N_B = \eta\left[H_N R_L \Delta t \pi\left(\frac{\Delta\theta_R}{2}\right)^2 A_R \Delta\lambda\right]\left(\frac{2\Delta z}{c}\right)\frac{1}{hc\upsilon_R}, \tag{3}$$

$$N_D = (C_N R_L \Delta t)\left(\frac{2\Delta z}{c}\right), \tag{4}$$

where η is the receiver efficiency, τ_L is the atmospheric transmission at the transmitted laser frequency υ_{L}, τ_{R} is the atmospheric transmission at the detected frequency υ_R, E_L is the laser energy per pulse (J), R_L is the repetition rate of the laser (s^{-1}), $\rho(z)$ is the concentration of scatterers at altitude z (m^{-3}), σ_{eff} is the effective backscatter cross section at frequency υ_{L}, temperature T, and velocity V (m^2), h is Planck's constant, c is the speed of light, A_R is the area of the telescope (m^2), H_N is the background sky radiance (W m^{-2} $\mu\mathrm{m}^{-1}$ sr^{-1}), $\Delta\theta_R$ is the field of view of the receiver (rad), $\Delta\lambda$ is the bandwidth of the detector (μm), and C_N is the dark count rate for the detector (s^{-1}). The photon-counting process is statistical in nature (Engstrom 1980), and the photon count signal has a Poisson distribution, where the variance of the signal equals the expected or mean value of the signal (Papoulis and Pillai 2002). For a Poisson distribution with a large mean value the distribution is well approximated by a normal (or Gaussian) distribution (Papoulis and Pillai 2002). Thus, we can model a given photon count signal with expected value of N_{TOT} as a normal random variable of mean N_{TOT} and standard deviation $(N_{\mathrm{TOT}})^{1/2}$. For a perfect measurement with no background or detector signal (i.e., $N_B + N_D = 0$) and a signal of 20 counts (i.e., $N_S = N_{\mathrm{TOT}} = 20$), we expect the signal photon count to have an associated photon count uncertainty of 4.5 counts and a

relative uncertainty of 22%. The same signal with a background and detector signal of 63 counts (i.e., $N_B + N_D = 63$, $N_S = 20$, $N_{\mathrm{TOT}} = 83$) would have an associated photon count uncertainty of 9.1 counts, yielding a relative uncertainty of 46%.

If the sodium concentration and laser power remain constant for measurements at two frequencies—υ_{L1} and υ_{L2}—then from Eq. (2),

$$\frac{N_S(z, \upsilon_{L2}, T, V)}{N_S(z, \upsilon_{L1}, T, V)} = \frac{\sigma_{\mathrm{eff}}(\upsilon_{L2}, T, V)}{\sigma_{\mathrm{eff}}(\upsilon_{L1}, T, V)} \tag{5}$$

(where T is the temperature, and V is the wind velocity); the ratio of the photon counts equals the ratio of the effective scattering cross sections. Early sodium Doppler wind–temperature lidars made these measurements using Doppler-free spectroscopy to lock the laser line near the D_{2a} and D_{2b} peak frequencies υ_{D2a} and υ_{D2b}, as well as near the crossover frequency υ_{D2c}, midway between the peak frequencies (Bills et al. 1991). In these systems, the operators first tuned the laser to one frequency, where the lidar signal was integrated over multiple laser pulses, and then tuned the laser to another frequency, where the lidar signal was again integrated over multiple laser pulses. The ratios of the signals were then used to determine the temperature and/or wind. Due to the integration of the lidar signal at different frequencies, these measurements included inaccuracies resulting from variations in the sodium concentration, wind, and temperature on a time scale of minutes.

Acousto-optic modulation techniques have subsequently been developed that yield robust three-frequency lidar measurements (White 1999; Sherman 2002). The laser is locked to the deepest Lamb dip in the Doppler-free spectrum at a frequency υ_0, close to the frequency of the D_{2a} peak υ_{D2a} ($\upsilon_0 = \upsilon_{\mathrm{D2a}} - 10.4$ MHz; She and Yu 1995). The acousto-optic modulation then generates two shifted frequencies: υ_+ ($= \upsilon_0 + \Delta\upsilon_{\mathrm{AO}}$, $\Delta\upsilon_{\mathrm{AO}} = 630$ MHz) and υ_- ($= \upsilon_0 - \Delta\upsilon_{\mathrm{AO}}$). The laser frequency changes sequentially on a pulse-to-pulse basis (every 0.02 s), and thus avoids the inaccuracies resulting from variations in the sodium concentration that were inherent in early wind–temperature lidar systems. The characteristics of the CSU lidar system are presented in Table 1.

Based on three-frequency measurements, we can define ratios that are sensitive to temperature and wind velocity,

$$R_T = \frac{\sigma_{\mathrm{eff}}(\upsilon_+, T, V) + \sigma_{\mathrm{eff}}(\upsilon_-, T, V)}{2\sigma_{\mathrm{eff}}(\upsilon_0, T, V)}$$
$$R_V = \frac{\sigma_{\mathrm{eff}}(\upsilon_+, T, V) - \sigma_{\mathrm{eff}}(\upsilon_-, T, V)}{\sigma_{\mathrm{eff}}(\upsilon_0, T, V)}. \tag{6}$$

TABLE 1. Characteristics of CSU sodium Doppler wind–temperature lidar.

Laser pulse energy	20 mJ
Laser repetition rate*	50 Hz
Laser line width	120 MHz
Laser pulse length	5 ns
Laser beam divergence	0.9 mrad
υ_0**	−651.4 MHz
υ_+	−21.4 MHz
υ_-	−1281.4 MHz
Telescope diameter	35 cm

* Laser cycles through three frequencies (υ_0, υ_+, and υ_-), and so repetition rate at each frequency is 50/3 Hz.

** Frequencies are relative to sodium D2 wavelength of 589.1583 nm.

Contours of R_T and R_V for constant T and V are plotted in Fig. 1. From Fig. 1, we see that R_T is most sensitive to changes in temperature and R_V is most sensitive to changes in radial velocity. However, the contours show that the ratios R_T and R_V are also both dependent upon temperature and velocity. If R_T was independent of velocity and R_V was independent of temperature, then the contours would be straight horizontal and vertical lines.

From Eq. (1) the received photon count signal is proportional to the product of the effective scattering cross section and the sodium concentration. For a three-frequency sodium Doppler wind–temperature lidar that is rapidly tuned on a pulse-to-pulse basis, the sodium concentration cancels out, and we can express the ratios directly in terms of the photon count signals,

$$R_T = \frac{N_s(\upsilon_+) + N_s(\upsilon_-)}{2N_s(\upsilon_0)}$$
$$R_V = \frac{N_s(\upsilon_+) - N_s(\upsilon_-)}{N_s(\upsilon_0)}, \tag{7}$$

where $N(\upsilon_+)$, $N(\upsilon_-)$, and $N(\upsilon_0)$ are the photon count signals measured at frequencies of υ_+, υ_-, and υ_0 respectively. We can relate the expected signal photon counts at υ_+ and υ_- to the signal photon count at υ_0 as

$$N_S(\upsilon_+) = N_S(\upsilon_0)\frac{\sigma_{\mathrm{eff}}(\upsilon_+, T, V)}{\sigma_{\mathrm{eff}}(\upsilon_0, T, V)}$$
$$N_S(\upsilon_-) = N_S(\upsilon_0)\frac{\sigma_{\mathrm{eff}}(\upsilon_-, T, V)}{\sigma_{\mathrm{eff}}(\upsilon_0, T, V)}. \tag{8}$$

Using the characteristics of the CSU sodium Doppler lidar in Table 1, and assuming the volume in the sodium layer has a temperature T_0 (= 200 K) and a line-of-sight wind V_0 (= 0 m s^{-1}), we find that the effective scattering cross sections $\sigma_{\mathrm{eff}}(\upsilon_+)$, $\sigma_{\mathrm{eff}}(\upsilon_0)$, and $\sigma_{\mathrm{eff}}(\upsilon_-)$ have values of 4.06, 9.22, and 3.50 ($\times 10^{-16}$ m^2), respectively.

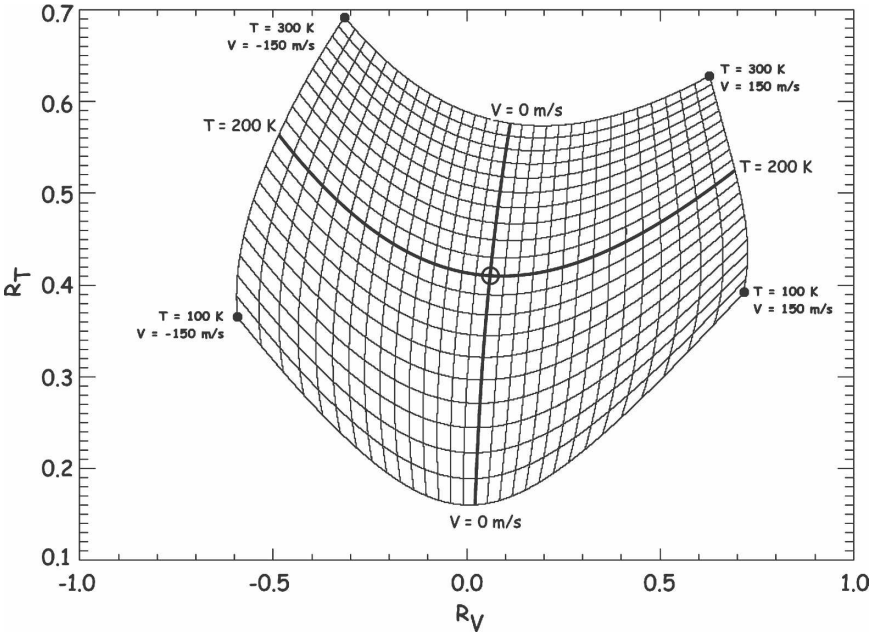

FIG. 1. The contours of R_T and R_V are plotted at intervals of 10 K and 10 m s^{-1}. Temperature varies between 100 and 300 K at a resolution of 0.1 K. Velocity varies between -150 and $+150$ m s^{-1} at a resolution of 0.1 m s^{-1}. The contours of R_T and R_V are plotted at 10 K and 10 m s^{-1}. The circle denotes the point (0.0604, 0.410) that corresponds to the ambient environmental conditions (200 K, 0 m s^{-1}).

The ratio of $\sigma_{\text{eff}}(v_+)/\sigma_{\text{eff}}(v_0)$ is equal to 0.440, and the ratio of $\sigma_{\text{eff}}(v_-)/\sigma_{\text{eff}}(v_0)$ is equal to 0.380. The value of R_T (i.e., R_{To}) is 0.410 and the value of R_V is (i.e., R_{Vo}) is 0.0604.

c. Inversion method

Retrieving temperature T and wind V is essentially interpolation from a table of unequally spaced pairs of temperature and velocity ratios (R_T, R_V). We calculate (R_T, R_V) pairs from Eq. (7) over a range of temperatures and winds (i.e., 100, 100.1, . . . , 300 K, and -150, -149.9, . . . , $+150$ m s^{-1}). We cover the resultant (R_T, R_V) surface with $n_{\text{TV}}(= n_T \times n_V) = 150 \times 100 = 150\,000$ rectangles with centers at (R_{Tij}, R_{Vij}) and introduce the following bilinear forms for T and V within each rectangle:

$$T = \alpha_{0ij} + \alpha_{1ij}(R_T - R_{Tij}) + \alpha_{2ij}(R_V - R_{Vij}) + \frac{1}{2}\alpha_{3ij}(R_T - R_{Tij})^2 + \frac{1}{2}\alpha_{4ij}(R_V - R_{Vij})^2 + \alpha_{5ij}(R_T - R_{Tij})(R_V - R_{Vij}),$$
$$V = \beta_{0ij} + \beta_{1ij}(R_T - R_{Tij}) + \beta_{2ij}(R_V - R_{Vij}) + \frac{1}{2}\beta_{3ij}(R_T - R_{Tij})^2 + \frac{1}{2}\beta_{4ij}(R_V - R_{Vij})^2 + \beta_{5ij}(R_T - R_{Tij})(R_V - R_{Vij}). \quad (9)$$

We find the αs and βs from a least squares fit to the generating values of (T, V) from the calculated values of (R_T, R_V). Thus, the inversion is reduced to evaluating two bilinear forms.

The accuracy of the inversion depends on the bilinear form and the size of the (R_T, R_V) rectangles. The mean rms error between the original (T, V) and the retrieved (T, V) from Eq. (9) is 0.003 K and 0.002 m s^{-1}. The rectangles span approximately 3 K and 2 m s^{-1}, so that when the amplitudes of the temperature and wind fluctuations are less than these values, the coefficients of a single (R_T, R_V) rectangle can be used to determine the fluctuations from analytic expressions. The lidar experiments in this study include cases with larger rms errors. Thus, we expect some disagreement between the results of single-rectangle analytical calculations and simulations that include variations over several rectangles.

TABLE 2. CSU sodium Doppler wind–temperature lidar signal levels at a measurement resolution of $\Delta t = 120$ s, $\Delta z = 150$ m.

Date	Time	Signal N_S (photon count)	Background and detector dark signal $N_B + N_D$ (photon count)	Sodium concentration (atoms m^{-3})	Relative error (%)
24 Jun 2002	1200 LT*	20	63	1.9×10^9	45.6
24 Jun 2002	0400 LT	150	0.5	2.8×10^9	8.2
6 Nov 2002	1200 LT	130	40	6.0×10^9	10.0
6 Nov 2002	0300 LT	1150	1.3	9.0×10^9	3.0

* LT = UTC − 7 h.

3. Scope of study

We determine the flux bias that would be measured by the lidar in the absence of heat flux. We assume that the sodium layer is at a constant temperature (200 K) and at rest (0 m s^{-1}).

We first consider experiments where there is no background skylight or detector signal (i.e., $N_D + N_B = 0$) and where $N_S(v_0)$ [$= N_{\mathrm{TOT}}(v_0)$] has an associated error of 0.1%, 0.5%, 1%, and 5% [i.e., $N_S(v_0) = 1 \times 10^6$, 4×10^4, 1×10^4, and 4×10^2, respectively]. These experiments represent the situation where the uncertainty in the measurements is determined by the statistics of the photon count signal. We term these cases the standard error experiments.

We then consider experiments based on actual photon count data from the CSU sodium Doppler wind–temperature lidar system. We tabulate these signal levels in Table 2. We consider measurements under the following four scenarios: midday in summer, nighttime in summer, midday in winter, and nighttime in winter. In summary, the sodium concentrations are 3 times smaller in summer than winter and the lidar signals are 8 times smaller in daytime than nighttime due to transmission losses associated with the additional narrowband optics required to reject sunlight. In 2002 the CSU lidar system employed a 0.35-m-diameter telescope. We scale the CSU lidar measurements to consider lidar systems employing a 1-, 1.8-, or 3.5-m-diameter telescope at a resolution of 2.5 min (150 s) and 480 m. These telescope diameters are representative of the receiver telescopes of contemporary single-telescope lidar systems. The diameter of the lidar telescope at the Arctic Lidar Observatory for Middle Atmosphere Research (ALOMAR) in Andoya, Norway (69°N, 16°E), is 1.8 m and that of the SOR telescope is 3.5 m. The resolution of the simulated lidar measurements is chosen to match the measurements of GY98. We term these cases the specific lidar system experiments.

4. Method of estimation of flux bias

a. Analytical approach

We can determine the expected values of the temperature $E(T)$ and wind $E(V)$ directly from Eq. (9). Also from Eq. (9) we can express the fluctuations in the measured temperature T' ($= T - T_0$) as the difference of two equations:

$$\begin{aligned} T' = T - T_0 = {} & \alpha_{1ij}[(R_T - R_{Tij}) - (R_{To} - R_{Tij})] + \alpha_{2ij}[(R_V - R_{Vij}) - (R_{Vo} - R_{Vij})] \\ & + \frac{1}{2}\alpha_{3ij}[(R_T - R_{Tij})^2 - (R_{To} - R_{Tij})^2] + \frac{1}{2}\alpha_{4ij}[(R_V - R_{Vij})^2 - (R_{Vo} - R_{Vij})^2] \\ & + \alpha_{5ij}[(R_T - R_{Tij})(R_V - R_{Vij}) - (R_{To} - R_{Tij})(R_{Vo} - R_{Vij})], \end{aligned} \tag{10}$$

where R_{To} and R_{Vo} are the values of R_T and R_V at T_0 and V_0, and the other terms have the same meaning as in Eq. (9). We linearize Eq. (10) to obtain the following expression for the temperature fluctuation:

$$T' = \alpha_{1ij}(R_T - R_{To}) + \alpha_{2ij}(R_V - R_{Vo}). \tag{11}$$

Similarly, we can express the fluctuations in the measured radial wind speed v' ($= V - V_0$),

$$v' = \beta_{1ij}(R_T - R_{To}) + \beta_{2ij}(R_V - R_{Vo}). \tag{12}$$

We can determine the flux f', defined as $f' = T' \times v'$, from Eqs. (11) and (12) as

$$\begin{aligned} f' = T'v' = {} & \gamma_1(R_T - R_{To})^2 + \gamma_2(R_V - R_{Vo})^2 \\ & + \gamma_3(R_T - R_{To})(R_V - R_{Vo}), \end{aligned} \tag{13}$$

where

$$\begin{aligned} \gamma_1 &= \alpha_{1ij}\beta_{1ij} \\ \gamma_2 &= \alpha_{2ij}\beta_{2ij} \\ \gamma_3 &= (\alpha_{1ij}\beta_{2ij} + \alpha_{2ij}\beta_{1ij}). \end{aligned} \tag{14}$$

We can express the expected value of the flux $E(f')$ as

$$E(f') = \gamma_1 E(R_T^2) + \gamma_2 E(R_V^2) + \gamma_3 E(R_T R_V) - (2\gamma_1 R_{To} + \gamma_3 R_{Vo}) E(R_T) - (2\gamma_2 R_{Vo} + \gamma_3 R_{To}) E(R_V) + \gamma_1 R_{To}^2 + \gamma_2 R_{Vo}^2 + \gamma_3 R_{To} R_{Vo}. \quad (15)$$

This expected flux is the bias in the flux measurement resulting from the statistical fluctuations in the lidar signal. We can think of the bias as an instrumental or apparent flux. From Eq. (15) we see that there are two contributions to the flux bias. First, there is the bias resulting from the cross correlation between R_T and R_V, based on the fact that they are calculated from a common triplet of photon count signals [$N(\upsilon_0)$, $N(\upsilon_+)$, $N(\upsilon_-)$]. This cross correlation is the source of the bias. The second contribution to the bias is due to the sensitivity of R_T to V and R_V to T (i.e., the magnitude of α_{2ij} and β_{1ij}). This sensitivity magnifies the bias. If R_T was independent of V and R_V was independent of T, the contours in Fig. 1 would have no curvature and would be vertical and horizontal. This independence would yield zero values of γ_1 and γ_2 and a value of $\gamma_3 = \alpha_{1ij}\beta_{2ij}$, and thus reduce the magnitude of the flux bias [Eq. (15)].

In principle, we can determine the expected value as well as all higher statistics of the flux bias if we know the probability density functions of R_T, R_V, $R_T R_V$, R_T^2, and R_V^2. Standard techniques yield a normal distribution for the sums and differences of normal random variables, a chi-squared distribution for squares of zero mean normal random variables, and a Cauchy distribution for ratios of zero mean normal random variables. However, the ratios of nonzero mean random variables do not, in general, have analytic probability density functions (Marsaglia 1965). Thus, we cannot determine analytic forms for the probability density functions of R_T, R_V, $R_T R_V$, R_T^2, and R_V^2, and we limit our attention to solving for the expected values of R_T, R_V, $R_T \times R_V$, R_T^2, and R_V^2. Because the photon count signals are independent random variables, we can express these expected values as

$$E(R_T) = \frac{1}{2} E[N_{\mathrm{TOT}}(\upsilon_+) + N_{\mathrm{TOT}}(\upsilon_-) - 2(N_D + N_B)] \times E\left[\frac{1}{N_{\mathrm{TOT}}(\upsilon_0) - (N_D + N_B)}\right],$$

$$E(R_V) = E[N_{\mathrm{TOT}}(\upsilon_+) - N_{\mathrm{TOT}}(\upsilon_-)] \times E\left[\frac{1}{N_{\mathrm{TOT}}(\upsilon_0) - (N_D + N_B)}\right],$$

$$E(R_T R_V) = \frac{1}{2} E\{N_{TOT}(\upsilon_+)^2 - N_{\mathrm{TOT}}(\upsilon_-)^2 - 2(N_D + N_B)[N(\upsilon_+) - N(\upsilon_-)]\} \times E\left\{\frac{1}{[N_{\mathrm{TOT}}(\upsilon_0) - (N_D + N_B)]^2}\right\}, \quad (16)$$

$$E(R_T^2) = \frac{1}{4} E\{[N_{\mathrm{TOT}}(\upsilon_+) + N_{\mathrm{TOT}}(\upsilon_-) - 2(N_D + N_B)]^2\} \times E\left\{\frac{1}{[N_{\mathrm{TOT}}(\upsilon_0) - (N_D + N_B)]^2}\right\},$$

$$E(R_V^2) = E\{[N_{\mathrm{TOT}}(\upsilon_+) - N_{\mathrm{TOT}}(\upsilon_-)]^2\} \times E\left\{\frac{1}{[N_{\mathrm{TOT}}(\upsilon_0) - (N_D + N_B)]^2}\right\}.$$

Using Eq. (16) we calculate the expected values by integrating the product of the function and the probability density function over the domain of the random variable (e.g., Papoulis and Pillai 2002) using the Romberg method as implemented in a standard computational package (Press et al. 1992; Research Systems 1999).

b. Monte Carlo simulation

We use a standard computational package to generate a sequence of the random variable X with a zero mean and unit standard deviation (Research Systems 1999). We then generate three photon count signals using standard linear transformation of the random variable X following Eq. (8),

$$N_S(\upsilon_0)_j = X_i[N_S(\upsilon_0) + N_D + N_B]^{1/2} + N_S(\upsilon_0)$$
$$N_S(\upsilon_+)_j = X_{i+1}\left[N_S(\upsilon_0)\frac{\sigma_{\mathrm{eff}}(\upsilon_+)}{\sigma_{\mathrm{eff}}(\upsilon_0)} + N_D + N_B\right]^{1/2} + N_S(\upsilon_0)\frac{\sigma_{\mathrm{eff}}(\upsilon_+)}{\sigma_{\mathrm{eff}}(\upsilon_0)}$$
$$N_S(\upsilon_-)_j = X_{i+2}\left[N_S(\upsilon_0)\frac{\sigma_{\mathrm{eff}}(\upsilon_-)}{\sigma_{\mathrm{eff}}(\upsilon_0)} + N_D + N_B\right]^{1/2} + N_S(\upsilon_0)\frac{\sigma_{\mathrm{eff}}(\upsilon_-)}{\sigma_{\mathrm{eff}}(\upsilon_0)}, \quad (17)$$

TABLE 3. Statistics of R_T and R_V.

Relative uncertainty in photon count		0.1%*	0.5%*	1.0%*	5.0%*
R_T	Mean	4.10×10^{-1}	4.10×10^{-1}	4.10×10^{-1}	4.11×10^{-1}
	Std dev	6.11×10^{-4}	3.06×10^{-3}	6.11×10^{-3}	3.08×10^{-2}
R_V	Mean	6.04×10^{-2}	6.04×10^{-2}	6.04×10^{-2}	6.06×10^{-2}
	Std dev	9.08×10^{-4}	4.54×10^{-3}	9.08×10^{-3}	4.56×10^{-2}

* Average of sample mean and std dev for 16 experiments of 1×10^6 samples.

for $j = 1, n$, and $i = 1, 3n - 2$. We point out that while the expected signal count varies with frequency, the expected background and detector count does not. As discussed in section 2, the effect of the background skylight and detector noise ($N_B + N_D$) is to increase the standard deviation of the signal (N_S). Finally, we generate R_T and R_V following Eq. (7), and we use the inversion method of Eq. (9) to determine the temperature and wind estimates (T, V). Thus, we determine n sample pairs of temperature and wind estimates (T_j, V_j) from n samples of the triplet $[N(\upsilon_0)_j, N(\upsilon_+)_j, N(\upsilon_-)_j]$.

We calculate the mean wind and temperature (i.e., T_0, V_0) and the fluctuating components of the wind and temperature (i.e., T', υ') for the n values. We then calculate the flux estimates as the product of the wind and temperature fluctuations (i.e., $f' = T' \times \upsilon'$) and the flux bias as the mean flux. We determine the accuracies of the mean temperature, wind, and flux estimates by repeating each experiment n_E times and calculating the sample standard deviation of the n_E estimates of the mean. We can calculate the number of samples required for the sample histogram of a normal random variable of zero mean and unit variance to converge to the probability density function within a given accuracy. The ratio of the standard deviation to the mean of the histogram scales as the square root of the number of samples. For values between 3.00 and 3.05 (i.e., between 3.00 and 3.05 standard deviations above the mean), the ratio of the standard deviation to the mean of the histogram is 23 for 10 samples and has a value of 7.0×10^{-2} for 10^6 samples. Thus, we require one million samples to guarantee that a sample histogram has converged within 7% to the probability density function at 3.00–3.05 standard deviations from the mean. In this study we present the histograms for R_T, R_V, T, υ', and f' for 16 experiments of 10^5 and 10^6 samples each.

5. Results

a. Statistics of R_T and R_V in standard error experiments

We conduct 16 experiments of 10^6 samples to determine the statistics of R_T and R_V. The mean and standard deviations are tabulated in Table 3. As expected, the standard deviations in R_T and R_V scale with the uncertainties in the photon counts, progressively increasing by the same factor as the uncertainties in the photon counts as the uncertainties increase from 0.1% to 5%. We determine the average histogram for the 16 experiments and fit normal curves to the histograms of R_T and R_V. The histograms of R_T and R_V and normal fits for the 1% standard error case are plotted in Fig. 2. The histograms are slightly asymmetric with differences of 6% or less between the standard deviation for values less than the mean and the standard deviation for values greater than the mean. The fits to the histograms of the populations have a linear correlation coefficient r, which is greater than 0.99. Under the assumption of a Student's t distribution, we estimate that the significance of these correlations is greater than 99% (Press et al. 1992; Pearson and Johnson 1968).

b. Statistics of temperature, wind, and flux measurements in standard error experiments

We conduct 16 experiments of 10^6 samples to determine the statistics of temperature T, wind V, and flux f'. The mean and standard deviations are tabulated in Table 4. As expected, the bias in the wind and flux estimates increases with the uncertainty in the photon count signals. The estimates of the flux biases for both the analytic and Monte Carlo approaches show the same behavior; the flux bias increases with the square of the relative uncertainty in the photon count signal. The cross-correlation coefficient of the temperature and velocity fluctuations is determined from the ratio of the mean flux bias to the product of the standard deviations of the temperature and velocity estimates. The net negative flux reflects the fact that the error fluctuations in temperature and velocity are correlated with a cross-correlation coefficient of 3%.

The histograms for T and V and their normal fits for the 1% standard error case are plotted in Fig. 3. The distributions are slightly asymmetric with differences of 13% or less in the standard deviation for values less

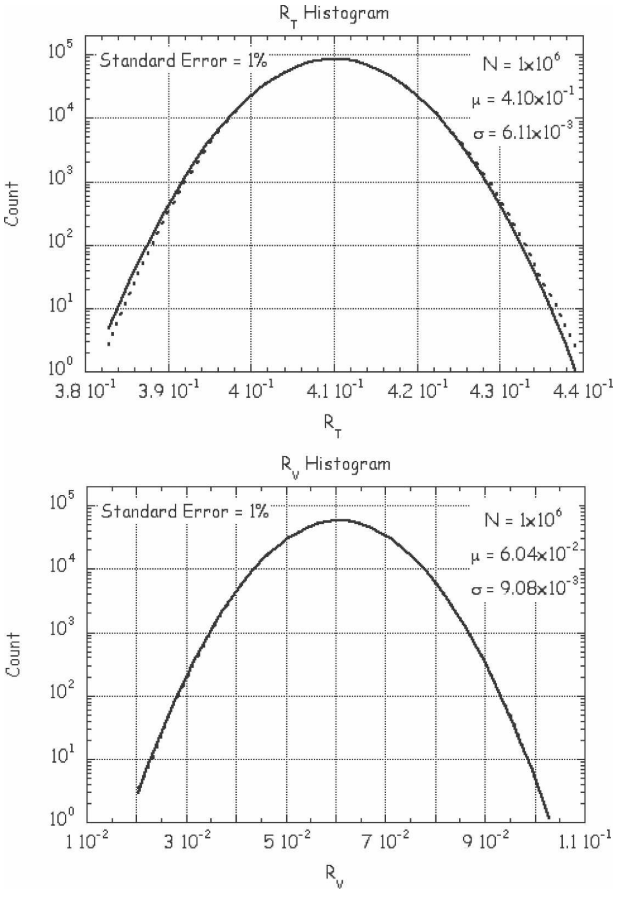

FIG. 2. Histogram of (a) temperature ratio R_T and (b) velocity ratio R_V measured by the lidar system for photon count errors of 1% (dashed). The histograms are each the average of 16 histograms, each of which contain 1×10^6 samples. Normal fits to each histogram are plotted for comparison (solid).

than and greater than the mean. The fits to the histograms of the populations have a linear correlation coefficient r that is greater than 0.99, and we conclude that the significance of the observed correlation is greater than 99%.

The flux f' does not behave as a normal random variable. The flux histogram in the 1% case has an asymmetric exponential distribution [$\sim\exp(-\lambda|x|)$] with a constant λ of 0.157 for positive flux values and 0.148 for the negative flux values (Fig. 4). The difference in the constants (0.009) is greater than the uncertainty in these fitted values (0.001). We observe this asymmetry, where the constant for positive flux has larger magnitude than the constant for the negative flux and the difference in the constants is greater than 3 times the uncertainty in the fit, in all cases. We find that the fits to the positive and negative portions of the flux histogram have a linear correlation coefficient r that is greater than 0.99, and the significance of this correlation is again greater than 99%. The asymmetry of the flux histogram reflects the negative bias in the flux estimates. We linearize the expressions for T', V', R_T, and R_V, and we obtain a bilinear form for f' in the random variables with contributions proportional to X_i^2, X_iX_{i+1}, X_iX_{i+2}, etc. We take appropriate linear combinations (Y_a, Y_b, and Y_c) of X_i, X_{i+1}, and X_{i+2}, and obtain a diagonal form, $f' = E_aY_a^2 + E_bY_b^2 + E_cY_c^2$. The Ys are again normal random variables with zero averages and unit standard deviations. We calculate $E_a = -3.775$, $E_b = 0$, and $E_c = 3.586$. This allows us to obtain the distribution of f' values from the integration of $\int\int dY_a dY_c\,(2\pi)^{-1}\exp(-Y_a^2 - Y_c^2)$ over appropriate limits. For photon count error of 1% we calculate that $\lambda = 0.146$ for $f' < 0$ and that $\lambda = 0.154$ for $f' > 0$. These values are in close agreement (less than 2% difference) with the values determined from the Monte Carlo approach.

c. *Statistics of temperature, wind, and flux measurements for specific lidar system experiments*

We need to scale the CSU lidar measurements to measurements made with lidar systems with 1-, 1.8-, and 3.5-m telescopes at a resolution of 2.5 min (150 s) and 480 m. Accordingly, we multiply the photon counts in Table 2 by factors of 32.6, 106, and 400, respectively. We tabulate the photon count uncertainties for each case in Table 5. We conduct simulations under the four sets of different geophysical conditions for 1- (Table 6), 1.8- (Table 7), and 3.5-m (Table 8) telescopes. In all of the simulations the uncertainties in the mean values are the value of the standard deviation divided by $(10^5)^{1/2}$, as expected.

In summary, for a 1-m telescope-based sodium Doppler wind–temperature lidar system the bias in the vertical heat flux measurements varies from -60.6 K m s^{-1} at midday in summer to -4.87×10^{-2} K m s^{-1} at night in winter. For a 1.8-m telescope-based sodium Doppler wind–temperature lidar system the bias in the vertical heat flux measurements varies from -18.0 K m s^{-1} at midday in summer to -1.47×10^{-2} K m s^{-1} at night in winter. For a 3.5-m telescope-based sodium Doppler wind–temperature lidar system the bias in the vertical heat flux measurements varies from -4.68 K m s^{-1} at midday in summer to -3.96×10^{-3} K m s^{-1} at night in winter. The source of the flux bias is due to the fact that the temperature and wind error fluctuations are correlated with a correlation coefficient of 2%–7%. The estimates of the flux bias from both the analytic and Monte Carlo approaches in Tables 6–8 show the same variation with geophysical conditions. Again, we find that the analytic estimates and the Monte Carlo

TABLE 4. Statistics of temperature, wind, and heat flux.

Relative uncertainty in photon count		0.1%*	0.5%**	1.0%*	5.0%**
Analytic					
T	Mean (K)	200.0	200.0	200.0	200.5
V	Mean (m s^{-1})	-3.55×10^{-5}	-1.48×10^{-3}	-6.01×10^{-3}	-1.53×10^{-1}
Flux	Mean (K m s^{-1})	-1.95×10^{-3}	-4.87×10^{-2}	-1.95×10^{-1}	-4.99
Monte Carlo					
T	Mean (K)	200.0	200.0	200.0	200.6
	Std dev (K)	0.3	1.5	3.0	15.2
	Std dev of mean (K)	2.8×10^{-4}	3.7×10^{-3}	2.8×10^{-3}	3.8×10^{-2}
V	Mean (m s^{-1})	1.85×10^{-5}	-5.07×10^{-4}	-5.34×10^{-3}	-1.43×10^{-1}
	Std dev (m s^{-1})	0.25	1.23	2.47	12.4
	Std dev of mean (m s^{-1})	2.29×10^{-4}	2.93×10^{-3}	2.28×10^{-3}	3.02×10^{-2}
Flux	Mean (K m s^{-1})	-1.90×10^{-3}	-4.52×10^{-2}	-1.92×10^{-1}	-4.98
	Std dev (K m s^{-1})	7.36×10^{-2}	1.84	7.38	193
	Std dev of mean (K m s^{-1})	7.21×10^{-5}	4.11×10^{-3}	7.12×10^{-3}	4.31×10^{-1}
Correlation (%)		2.5	2.5	2.6	2.6

* Average of sample mean and std dev for 16 experiments of 1×10^6 samples.
** Average of sample mean and std dev for 16 experiments of 1×10^5 samples.

estimates differ by amounts less than or equal to the uncertainty in the Monte Carlo estimates.

The performance of the lidar systems as a function of telescope diameter is summarized in Fig. 5, wherein we plot the magnitude of the flux bias against the telescope diameter for each of the four geophysical scenarios. We plot the following three horizontal lines for comparison: the magnitude vertical heat flux (2.29 K m s^{-1}) measured at SOR by GY98, 10% of the GY98 SOR measurement (0.229 K m s^{-1}), and the flux bias for the 1% standard case (0.192 K m s^{-1}). Clearly, the summer midday measurements provide the greatest challenge, where the measurement biases are greater than the actual flux for lidar systems employing 1- and 1.8-m telescopes. At midday in summer the 3.5-m telescope yields a bias that is 70% of the actual flux measured by GY98. However, under all of the other conditions (i.e., summer nighttime, winter midday, and winter nighttime) the flux bias is less than 10% of the value measured by GY98. The 1.8-m telescope-based system yields biases that are less than 10% of the actual flux at night in all seasons. The 1-m telescope-based system yields biases that are less than 10% of the actual flux only at night in winter. The cross-correlation coefficients of 2%–7% are less than the values of 12% reported by GY98.

d. Comparison with method of GY98

As discussed earlier, GY98 employed the sodium Doppler wind–temperature lidar technique to make vertical heat flux measurements at SOR. They defined R_T and R_V as

$$R_T = \frac{N_S(\upsilon_+) + N_S(\upsilon_-)}{[1 + N_S(\upsilon_0)]},$$
$$R_V = \frac{N_S(\upsilon_-)}{[1 + N_S(\upsilon_+)]}. \quad (18)$$

We have simulated the lidar experiment using these definitions. The values of R_T and R_V are different (with mean values of 0.820 and 0.863, respectively) from the values we have calculated using the definition given in Eq. (7) (Table 3). In our simulations we compare the statistics of the temperature, wind, and flux measurements using GY98's method [Eq. (18)] and the method used in this study [Eq. (7)]. The differences in the temperature estimates are less than 1% of the mean and 1% of the standard deviation. The differences in the mean values of the wind estimates are less than 3% of the standard deviation. Finally, we find that the mean value of the flux is negative and differs from our definition by less than 6% of the mean and 1% of the standard deviation.

GY98 estimate a value of 8×10^{-5} K m s^{-1} for the magnitude of the bias associated with a photon count signal level of 3.0×10^4 counts for measurements at a resolution of 480 m and 150 s. The current study indicates that sodium Doppler wind–temperature lidar measurements of the vertical heat flux have an instrumental flux bias of -4×10^{-3} K m s^{-1} for a system employing a transmitter equivalent to the CSU lidar system and a 3.5-m telescope at the same resolution at nighttime in winter. This bias is associated with a measurement resolution and a photon count signal level of 4.6×10^5 counts, and a background and dark count signal of 520 counts. The GY98 estimate does not in-

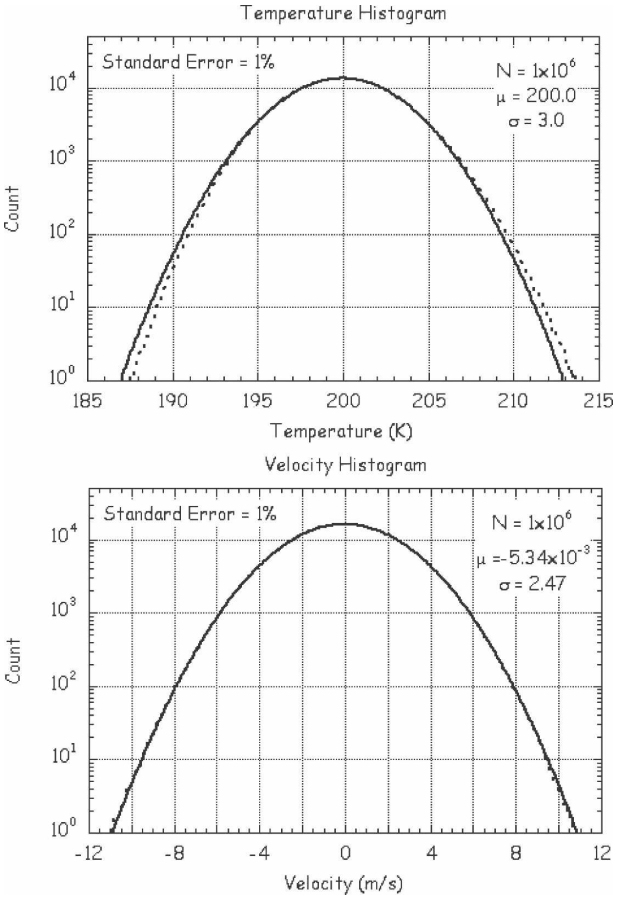

FIG. 3. Histogram of (a) temperature and (b) velocity measured by the lidar system for photon count errors of 1% (dashed). The histograms are each the average of 16 histograms, each of which contain 1×10^6 samples. Normal fits to each histogram are plotted for comparison (solid).

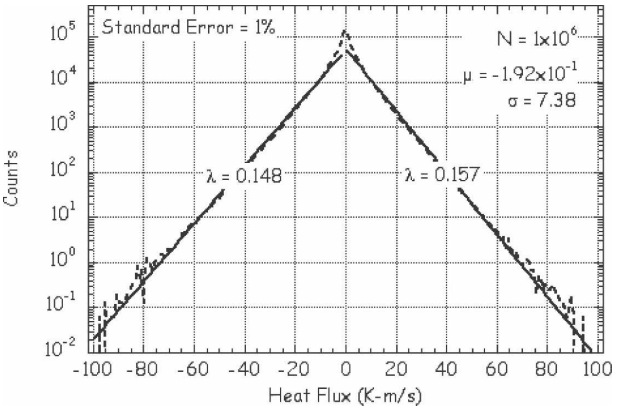

FIG. 4. Histogram of fluxes measured by the lidar system for photon count errors of 1% (dashed). The histogram is the average of 16 histograms, each of which contain 1×10^6 samples. Exponential fits to the positive and negative side of the histogram are plotted for comparison (solid). The flux histogram has an asymmetric exponential distribution [$\sim\exp(-\lambda|x|)$] with a constant of 0.157 for positive flux values and 0.148 for the negative flux values. The histogram is calculated over 201 successive 1 K m s^{-1} intervals distributed between -100 and $+100$ K m s^{-1}.

clude the effect of correlation of R_T with V and R_V with T [see their Eqs. (A17)–(A23)], and hence is a lower bound on the flux bias. Our study shows that for the measurement conditions at SOR the actual bias in the heat flux is greater than that reported by GY98, but is still be much smaller than the actual vertical heat flux.

6. Discussion

While the flux bias decreases with increasing signal level, the lidar signal is not infinitely scalable. From Eqs. (2) and (3) the accuracy of the lidar measurements is improved by increasing the laser pulse energy (increasing N_S) or reducing the laser beam divergence (decreasing N_B). However, saturation effects in the mesospheric metal layer limit the amplitude of the lidar signal (Megie et al. 1978). As the energy flux of the laser pulse is increased (by increasing the pulse energy or decreasing the beam divergence), a higher fraction of the sodium atoms are excited by the leading edge of the pulse and, due to the nonzero lifetime of the excited state (~16 ns), are unable to interact with the photons in the trailing edge of the pulse. Under these conditions, the sodium layer is saturated and the actual lidar signal is less than expected. Following Megie et al., we use the system parameters in Table 1 and find that the lidar signals are over 99.5% of the unsaturated values. Decreasing the laser beam divergence to 0.2 (0.1) mrad decreases the background skylight by a factor of 20 (81) and yields signals that are over 90.7% (69.3%) of the unsaturated values.

Current lidar receiver signals are also limited by the (nonzero) width of the electronic pulses generated in the photomultiplier tubes of the lidar receiver. Typical pulse widths of 5 ns correspond to maximum count rates of 200 MHz (Engstrom 1980). The data in Table 2 indicate count rates in winter of 5.75×10^5 Hz and count rates in summer of 4.15×10^4 Hz. These count

TABLE 5. Doppler wind–temperature lidar signal measurement errors at a measurement resolution of $\Delta t = 150$ s, $\Delta z = 480$ m.

	Relative photon count error (%)		
Telescope diameter	1 m	1.8 m	3.5 m
Summer midday	8.0	4.4	2.3
Summer night	1.4	0.8	0.4
Winter midday	1.8	1.0	0.5
Winter night	0.5	0.3	0.2

TABLE 6. Statistics of T, V, and heat flux for CSU lidar and 1-m telescope.

		Summer midday*	Summer night*	Winter midday*	Winter night*
Analytic					
T	Mean (K)	200.9	200.0	200.1	200.0
V	Mean (m s^{-1})	-6.49×10^{-1}	-1.24×10^{-2}	-2.23×10^{-2}	-1.59×10^{-3}
Flux	Mean (K m s^{-1})	-60.3	-4.07×10^{-1}	-1.30	-5.23×10^{-2}
Monte Carlo					
T	Mean (K)	200.3	200.0	200.1	200.0
	Std dev (K)	30.0	4.3	5.7	1.5
	Std dev of mean (K)	1.0×10^{-1}	1.0×10^{-2}	1.5×10^{-2}	3.8×10^{-3}
V	Mean (m s^{-1})	-5.96×10^{-1}	-9.54×10^{-3}	-1.83×10^{-2}	-5.79×10^{-4}
	Std dev (m s^{-1})	29.0	3.55	5.04	1.28
	Std dev of mean (m s^{-1})	7.09×10^{-2}	8.46×10^{-3}	1.20×10^{-2}	3.03×10^{-3}
Flux	Mean (K m s^{-1})	-60.6	-3.84×10^{-1}	-1.25	-4.87×10^{-2}
	Standard deviation (K m s^{-1})	926	15.2	28.9	1.97
	Std dev of mean (K m s^{-1})	1.70	3.37×10^{-2}	6.34×10^{-2}	4.40×10^{-3}
Correlation (%)		7.0	2.5	4.4	2.5

* Average of sample mean and std dev for 16 experiments of 1×10^5 samples.

rates scale to 57.5 and 4.15 MHz for a single 3.5-m telescope receiver. The summertime measurements could be further improved by using larger telescopes. The results presented in Tables 6–8 suggest that the bias in the flux measurement decreases proportionally to the photon count signal level (or equivalently the telescope area). Increasing the signal level by a factor of 10 would yield an acceptable count rate and reduce the flux bias in daytime summer measurements to -0.16 K m s^{-1}, or 7% of the actual flux measured by GY98. Use of receivers with multiple telescopes and multiple detectors would also alleviate the problem at the cost of extra experimental resources and optical alignment and calibration efforts.

Our study highlights the impact of the geophysical conditions on flux measurements. The column abundance of the sodium layer has a strong seasonal variation with maximum in winter and minimum in summer. This seasonal variation is more pronounced at high latitudes than low latitudes; thus, we expect that summertime measurements in the polar regions will be the most challenging. Summertime polar measurements are based on resonance signals that are approximately 5 times lower than those expected at midlatitudes and are made under daylight conditions (Gardner et al. 2005). We scale the summer midday measurements from Table 2 and find that the expected relative photon count errors in 150-s, 480-m measurements would be 36%, 20%, and 10% for the 1-, 1.8-, and 3.5-m telescope-based lidar systems, respectively.

The biases that we have computed in this study are associated with the CSU sodium Doppler wind–

TABLE 7. Statistics of T, wind, and heat flux for CSU lidar and 1.8-m telescope.

		Summer midday*	Summer night*	Winter midday*	Winter night*
Analytic					
T	Mean (K)	200.3	200.0	200.0	200.0
V	Mean (m s^{-1})	-1.96×10^{-1}	-3.79×10^{-3}	-6.84×10^{-3}	-4.71×10^{-4}
Flux	Mean (K m s^{-1})	-18.2	-1.25×10^{-1}	-3.99×10^{-1}	-1.61×10^{-2}
Monte Carlo					
T	Mean (K)	200.3	200.0	200.0	200.0
	Std dev (K)	16.9	2.4	3.2	0.9
	Std dev of mean (K)	4.5×10^{-2}	5.8×10^{-3}	8.0×10^{-3}	2.1×10^{-3}
V	Mean (m s^{-1})	-1.82×10^{-1}	-2.23×10^{-3}	-4.63×10^{-3}	7.64×10^{-5}
	Std dev (m s^{-1})	16.0	1.97	2.79	7.08×10^{-1}
	Std dev of mean (m s^{-1})	3.85×10^{-2}	4.68×10^{-3}	6.63×10^{-3}	1.68×10^{-3}
Flux	Mean (K m s^{-1})	-18.0	-1.18×10^{-1}	-3.84×10^{-1}	-1.47×10^{-2}
	Std dev (K m s^{-1})	275	4.67	8.85	6.04×10^{-1}
	Std dev of mean (K m s^{-1})	5.97×10^{-1}	1.04×10^{-2}	1.96×10^{-2}	1.36×10^{-3}
Correlation (%)		6.7	2.5	4.3	2

* Average of sample mean and std dev for 16 experiments of 1×10^5 samples.

TABLE 8. Statistics of temperature, wind, and heat flux for CSU lidar and 3.5-m telescope.

		Summer midday*	Summer night*	Winter midday*	Winter night*
Analytic					
T	Mean (K)	200.1	200.0	200.0	200.0
V	Mean (m s^{-1})	-5.15×10^{-2}	-9.87×10^{-4}	-1.79×10^{-3}	-1.07×10^{-4}
Flux	Mean (K m s^{-1})	-4.79	-3.31×10^{-2}	-1.06×10^{-1}	-4.26×10^{-3}
Monte Carlo					
T	Mean (K)	200.1	200.0	200.0	200.0
	Std dev (K)	8.6	1.2	1.6	0.4
	Std dev of mean (K)	2.3×10^{-2}	3.0×10^{-3}	4.1×10^{-3}	1.1×10^{-3}
V	Mean (m s^{-1})	-4.49×10^{-2}	-1.93×10^{-4}	-6.70×10^{-4}	1.64×10^{-4}
	Std dev (m s^{-1})	8.20	1.01	1.44	3.65×10^{-1}
	Std dev of mean (m s^{-1})	1.95×10^{-2}	2.40×10^{-3}	3.41×10^{-3}	8.65×10^{-4}
Flux	Mean (K m s^{-1})	-4.68	-3.06×10^{-2}	-1.01×10^{-1}	-3.96×10^{-3}
	Std dev (K m s^{-1})	71.0	1.24	2.34	1.61×10^{-1}
	Std dev of mean (K m s^{-1})	1.54×10^{-1}	2.76×10^{-3}	5.21×10^{-3}	3.60×10^{-4}
Correlation (%)		6.6	2.5	4.4	2.7

* Average of sample mean and std dev for 16 experiments of 1×10^5 samples.

temperature lidar. The CSU lidar uses a dye laser with a three-frequency technique that incorporates acousto-optic modulation to rapidly switch between laser frequencies. Gardner (2004) has reviewed three-frequency lidar techniques for application in a variety of metals (e.g., sodium, iron, potassium, and calcium). Iron lidar systems have attracted increasing attention because they can employ solid-state alexandrite lasers, rather than dye lasers, to measure the temperature of the mesospheric iron layer (Chu et al. 2002). Gardner (2004) presents different R_T and R_V metrics for such three-frequency techniques that yield different flux biases. The flux bias will change with the acousto-optic frequency shift because the relative curvature of the (R_T, R_V) surface (Fig. 1) will be altered. Furthermore, the flux bias will vary with the seasonal variation in environmental conditions as curvature of the (R_T, R_V) surface varies with temperature. In principle we can choose the acousto-optic frequency shift to minimize the flux bias under different environmental conditions. Lautenbach and Höffner (2004) have presented temperature measurements from an iron resonance lidar that employed a frequency-scanning, rather than a three-frequency, approach. We expect that such a system could be developed to make optimized measurements of the heat fluxes with minimum biases.

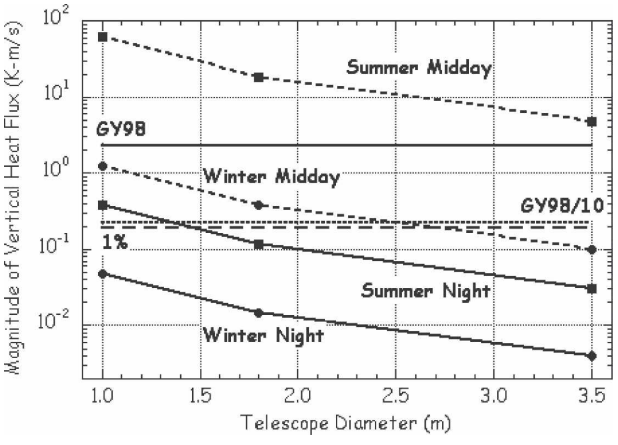

FIG. 5. Magnitude of bias in vertical heat flux measured by sodium Doppler wind–temperature lidar systems as a function of telescope diameter under different geophysical conditions: summer midday (dash square), winter midday (dash circle), summer night (solid, square), and winter night (solid circle). The vertical heat flux measured by GY98 (GY98) (horizontal solid line at 2.29 K m s^{-1}), the value of 10% of the vertical heat flux measured by GY98 (GY98/10) (horizontal short dash line at 0.229 K m s^{-1}), and the flux bias for 1% measurements (Table 4) (horizontal long dash line at 0.192 K m s^{-1}) are plotted for comparison.

7. Conclusions

In this study we have analyzed sodium Doppler wind–temperature lidar measurements of the vertical heat flux. We used experimental data from current sodium Doppler wind–temperature systems to determine the statistical parameters of the photon counting process associated with lidar measurements in both winter and summer, day and night, with a range of telescopes (1-, 1.8-, and 3.5-m diameter). We considered the flux bias that would be estimated from wind–temperature measurements of a sodium layer at rest that has a constant temperature. The variability in the measurements is due to the Poisson statistics of the photon-counting process inherent in the measurement technique.

We find a cross-correlation coefficient of 2%–7% be-

tween the lidar wind and temperature estimates. We find that the biases vary from -3.96×10^{-3} K m s^{-1} for wintertime measurements at night with a 3.5-m telescope to -60.6 K m s^{-1} for summertime measurements at midday with a 1-m telescope. We find that during winter at night all three systems (1-, 1.8-, and 3.5-m diameter) yield biases in their heat flux measurements that are less than 10% of the reported value of the heat flux. During summer at night the 1.8- and 3.5-m systems yield biases in their heat flux measurements that are less than 10% of the reported vertical heat flux of 2.3 K m s^{-1}. During winter at midday the 3.5-m system yields biases in their heat flux measurements that are less than 10% of the geophysical value. During summer at midday all of the systems yield biases that are greater than the geophysical value of the heat flux.

We have limited our analysis to that of the sodium Doppler wind–temperature lidar system that is currently operated at CSU. Lidar systems employing other mesospheric metals (e.g., iron), different laser technologies (e.g., alexandrite), and different temperature and wind metrics are under development in the middle-atmosphere lidar community. However, these other lidar systems also employ photon-counting techniques with the same general class of bilinear inversion methods. We have presented an analysis that provides a general framework for determining the flux biases associated with these systems.

Acknowledgments. This work was initiated while two of the authors (LS and RLC) spent a semester in residence at the Department of Physics at the Colorado State University. LS and RLC thank Erich Becker, Josef Höffner, Devin S. Johnson, and David E. Newman for helpful discussion. We thank two anonymous reviewers for providing insightful and critical reviews of the paper. LS and RLC acknowledge support from the NSF CEDAR program under Grants ATM-99-79454 and ATM-01-22995. DAK and CS acknowledge support from the NSF CEDAR program under Grant ATM-05-45221 and NASA under Grant NAG5-10076.

REFERENCES

Andrews, D. G., J. R. Holton, and C. B. Leovy, 1987: *Middle Atmosphere Dynamics*. Academic Press, 489 pp.

Arnold, K. S., and C. Y. She, 2003: Metal fluorescence lidar (light detection and ranging) and the middle atmosphere. *Contemp. Phys.,* **44,** 35–49.

Becker, E., 2004: Direct heating rates associated with gravity wave saturation. *J. Atmos. Solar-Terr. Phys.,* **66,** 633–696.

Bills, R. E., C. S. Gardner, and S. F. Franke, 1991: Na Doppler/temperature lidar: Initial mesopause region observations and comparison with the Urbana medium frequency radar. *J. Geophys. Res.,* **96,** 22 701–22 707.

Chu, X., and G. C. Papen, 2005: Resonance fluorescence lidar for measurements in the middle and upper atmosphere. *Laser Remote Sensing,* T. Fujii and T. Fukuchi, Eds., CRC Press, 179–432.

——, ——, W. Pan, C. S. Gardner, and J. Gelbwachs, 2002: Fe Boltzmann temperature lidar: Design, error analysis and first results from North and South Poles. *Appl. Opt.,* **41,** 4400–4410.

Engstrom, R. W., 1980: *RCA Photomultiplier Handbook*. Radio Corporation of America, 180 pp.

Fricke, K. H., and U. von Zahn, 1985: Mesopause temperatures derived from probing the hyperfine structure of the D2 resonance line of sodium by lidar. *J. Atmos. Terr. Phys.,* **47,** 499–512.

Fritts, D. C., and M. J. Alexander, 2003: Gravity wave dynamics and effects in the middle atmosphere. *Rev. Geophys.,* **41,** 1003, doi:10.1029/2001RG000106.

Gardner, C. S., 2004: Performance capabilities of middle-atmosphere temperature lidars: Comparison of Na, Fe, K, Ca, Ca+, and Rayleigh systems. *Appl. Opt.,* **43,** 4941–4956.

——, and W. Yang, 1998: Measurements of the dynamical cooling rate associated with the vertical transport of heat by dissipating gravity waves in the mesopause region at the Starfire Optical Range, New Mexico. *J. Geophys. Res.,* **103,** 16 909–16 926.

——, D. C. Senft, and K. H. Kwon, 1988: Lidar observations of substantial sodium depletion in the summertime Arctic mesosphere. *Nature,* **332,** 142–144.

——, Y. Zhao, and A. Z. Liu, 2002: Atmospheric stability and gravity wave dissipation in the mesopause region. *J. Atmos. Solar-Terr. Phys.,* **64,** 923–929.

——, J. M. C. Plane, W. Pan, T. Vondrak, B. J. Murray, and X. Chu, 2005: Seasonal variations of the Na and Fe layers at the South Pole and their implications for the chemistry and general circulation of the polar mesosphere. *J. Geophys. Res.,* **110,** D10302, doi:10.1029/2004JD005670.

Gibson, A. J., L. Thomas, and S. K. Bhattachacharyya, 1979: Laser observations of the ground-state hyperfine structure of sodium and of temperatures in the upper atmosphere. *Nature,* **281,** 131–132.

Houghton, J. T., 1978: The stratosphere and mesosphere. *Quart. J. Roy. Meteor. Soc.,* **104,** 1–29.

Huang, T. Y. W., and A. K. Smith, 1991: The mesospheric diabatic circulation and the parameterized thermal effect of gravity wave breaking on the circulation. *J. Atmos. Sci.,* **48,** 1093–1111.

Johnson, R. M., and T. L. Killeen, Eds., 1995: *The Upper Mesosphere and Lower Thermosphere: A Review of Experiment and Theory. Geophys. Monogr.,* Vol. 87, Amer. Geophys. Union, 356 pp.

Kudeki, E., and S. J. Franke, 1998: Statistics of momentum flux estimation. *J. Atmos. Solar-Terr. Phys.,* **60,** 1549–1553.

Lautenbach, J., and J. Höffner, 2004: Scanning iron temperature lidar for mesopause temperature observation. *Appl. Opt.,* **43,** 4559–4563.

Liu, A. Z., and C. S. Gardner, 2005: Vertical heat and constituent transport in the mesopause region by dissipating gravity waves at Maui, Hawaii (20.7°N) and Starfire Optical Range, New Mexico (35°N). *J. Geophys. Res.,* **110,** D09S13, doi:10.1029/2004JD004965.

Marsaglia, G., 1965: Ratios of normal random variables and ratios of sums of uniform variables. *J. Amer. Stat. Assoc.,* **60,** 193–204.

Megie, G., F. Bos, J. E. Blamont, and M. L. Chanin, 1978: Simultaneous nighttime lidar measurements of atmospheric sodium and potassium. *Planet. Space Sci.,* **26,** 27–35.

Papoulis, A., and S. U. Pillai, 2002: *Probability, Random Variables, and Stochastic Processes.* 4th ed. McGraw Hill, 852 pp.

Pearson, E. S., and N. L. Johnson, 1968: *Tables of the Incomplete Beta-function.* 2nd ed. Cambridge University Press, 505 pp.

Plane, J. M. C., 1991: The chemistry of meteoric metals in the earth's upper atmosphere. *Int. Rev. Phys. Chem.,* **10,** 55–106.

Press, W. H., S. A. Teukolsky, W. T. Vetterling, and B. P. Flannery, 1992: *Numerical Recipes in FORTRAN: The Art of Scientific Computing.* 2nd ed. Cambridge University Press, 963 pp.

Research Systems, 1999: RANDOMN. IDL Version 5.3.

Schoeberl, M. R., D. F. Strobel, and J. P. Apruzese, 1983: A numerical model of gravity wave breaking and stress in the mesosphere. *J. Geophys. Res.,* **88,** 5249–5259.

She, C. Y., and J. R. Yu, 1995: Doppler-free saturation fluorescence spectroscopy of Na atoms for atmospheric applications. *Appl. Opt.,* **34,** 1063–1075.

——, H. Latifi, J. R. Yu, R. J. Alvarez II, R. E. Bills, and C. S. Gardner, 1990: Two-frequency lidar technique for mesospheric Na temperature measurements. *Geophys. Res. Lett.,* **17,** 929–932.

——, J. R. Yu, H. Latifi, and R. E. Bills, 1992: High-spectral-resolution fluorescence light detection and ranging for mesospheric sodium temperature measurements. *Appl. Opt.,* **31,** 2095–2106.

Sherman, J. P., 2002: Mesopause region thermal and dynamical studies based on simultaneous temperature, zonal and meridional wind measurements with an upgraded sodium fluorescence lidar. Ph.D. dissertation, Colorado State University, 137 pp.

Siskind, D. E., S. D. Eckermann, and M. E. Summers, Eds., 2000: *Atmospheric Science across the Stratopause. Geophys. Monogr.,* Vol. 123, Amer. Geophys. Union, 342 pp.

Stull, R. B., 1988: *An Introduction to Boundary Layer Meteorology*. Kluwer Academic, 666 pp.

Thorsen, D., S. J. Franke, and E. Kudeki, 2000: Statistics of momentum flux estimation using the dual coplanar beam technique. *Geophys. Res. Lett.,* **27,** 3193–3196.

Vincent, R. A., and I. M. Reid, 1983: HF Doppler measurements of mesospheric gravity wave momentum fluxes. *J. Atmos. Sci.,* **40,** 1321–1333.

Walterscheid, R. L., 1981: Inertio-gravity wave induced accelerations of mean flow having an imposed periodic component: Implications for tidal observations in the meteor region. *J. Geophys. Res.,* **86,** 9698–9706.

Wang, D.-Y., and D. C. Fritts, 1990: Mesospheric momentum fluxes observed by the MST radar at Poker Flat, Alaska. *J. Atmos. Sci.,* **47,** 1512–1521.

White, M. A., 1999: A frequency-agile Na lidar for the measurement of temperature and velocity in the mesopause region. Ph.D. dissertation, Colorado State University, 123 pp.